

Detecting Comma-shaped Clouds for Severe Weather Forecasting using Shape and Motion

Xinye Zheng, Jianbo Ye, Yukun Chen, Stephen Wistar, Jia Li,
Jose A. Piedra-Fernández, Michael A. Steinberg, and James Z. Wang

Abstract—Meteorologists use shapes and movements of clouds in satellite images as indicators of several major types of severe storms. Satellite imagery data are in increasingly higher resolution, both spatially and temporally, making it impossible for humans to fully leverage the data in their forecast. Automatic satellite imagery analysis methods that can find storm-related cloud patterns as soon as they are detectable are in demand. We propose a machine learning and pattern recognition based approach to detect “comma-shaped” clouds in satellite images, which are specific cloud distribution patterns strongly associated with the cyclone formulation. In order to detect regions with the targeted movement patterns, our method is trained on manually annotated cloud examples represented by both shape and motion-sensitive features. Sliding windows in different scales are used to ensure that dense clouds will be captured, and we implement effective selection rules to shrink the region of interest among these sliding windows. Finally, we evaluate the method on a hold-out annotated comma-shaped cloud dataset and cross-match the results with recorded storm events in the severe weather database. The validated utility and accuracy of our method suggest a high potential for assisting meteorologists in weather forecasting.

Index Terms—Severe weather forecasting, comma-shaped cloud, Meteorology, satellite images, pattern recognition, AdaBoost.

I. INTRODUCTION

Severe weather events such as thunderstorms can cause significant losses in property and lives. Many countries and regions suffer from storms regularly, leading to a global issue. Severe storms also kill over 20 people per year in the U.S. [1]. The U.S. government has invested more than 0.5 billion dollars [2] to the research on detecting and forecasting storms. Billions of dollars have been invested for a modern weather satellite equipping with high-definition cameras.

The fast pace of developing computing power and increasingly higher definition satellite images precipitate us into re-examining the conventional efforts regarding storm forecast, such as bare eye interpretation of satellite images [3]. Bare eye image interpretation by experts requires domain knowledge of cloud involvements and, for a variety of reasons, may cause misses or delays of extreme weather forecasting. Moreover, the enhancements from the latest satellites, which deliver images in real-time at a very high resolution, demand stingiest processing speed. This encourages us to explore the opportunities by applying modern learning schema on forecasting storms in order to aid meteorologists in interpreting visual clues of storms from satellite images.

Evident visual patterns appear in the satellite images with the cyclone formation in the mid-latitude area. This feature

is named the comma-shaped cloud pattern [4], which refers to a typical cloud distribution strongly associated with the mid-latitude cyclonic storm systems. As shown in Fig. 1, the cloud shield has the appearance of a comma mark in the northern hemisphere, where the “tail” is formed with the warm conveyor belt extending to the east, and the “head” is formed within the range where the cold conveyor belt forms in the northeast direction. The dry-tongue jet forms a cloudless zone between the comma head and the comma tail. It gets the name because the stream is oriented from the dry upper troposphere and it has not achieved saturation before ascending over the low-pressure center. The comma-shaped cloud feature is strongly associated with many types of extratropical cyclones, including hail, thunderstorm, high wind, blizzards, and low-pressure systems. Consequently, we can observe severe events like snow, ice, rain, and thunderstorms around this visual feature [5].

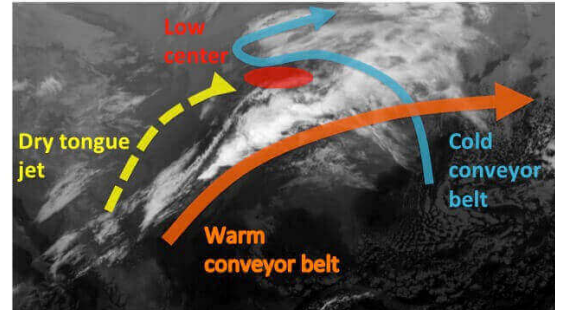


Fig. 1. An example of the satellite image with the comma-shaped cloud. This image is taken at 03:15:19 UTC on Dec 15, 2011 from the fourth channel of the GOES-N weather satellite.

To capture the comma-shaped cloud pattern accurately, meteorologists have to read different weather data and many satellite images simultaneously, leading to inaccurate or untimely detection of suspected visual signals. Such manual procedures are not scalable if we are to leverage all available weather data, which are increasingly of visual form and with high resolution. Negligence in the manual interpretation of weather data can lead to serious consequences. Automating this process, through creating intelligent computer-aided tools, can potentially benefit the analysis of historical data and make meteorologists’ forecasting effort less intensive. This philosophy is persuasive in the computer vision and multimedia community, where images in modern image retrieval and annotation systems are indexed by not only metadata such as author and timestamp, but also semantic annotations and contextual relatedness based on the pixel content [6], [7].

We propose a machine learning and pattern recognition based approach to detect comma-shaped clouds from satellite images. The comma-shaped cloud patterns, which have been manually searched and indexed by meteorologists, can be

X. Zheng, J. Ye, Y. Chen, J. Li and J. Wang are with The Pennsylvania State University, University Park, PA, USA. Correspondence should be addressed to X. Zheng and J. Z. Wang (e-mails: {xvz5220, jwang}@psu.edu).

S. Wistar and M. Steinberg are with Accuweather Inc., USA.

J. Piedra-Fernández is with University of Almería, Spain.

automatically detected by computerized systems using our proposed approach. We take advantages of large satellite image data set in the historical archive to train the model and demonstrate the effectiveness of our method in a manually annotated comma-shaped cloud dataset. As we will show in the later part of this paper, this method can also help meteorologists to effectively forecast storms, due to the strong connection of comma-shaped cloud and storm formation.

While all comma-shaped clouds resemble the shape of a comma mark to some extent, the appearance and size of one such cloud can be very different from those of another. This makes conventional object detection or pattern matching techniques developed in computer vision inappropriate because they often assume a well-defined object shape (e.g. a face) or pattern (e.g. the skin texture of a zebra).

The key visual cues that human experts use with their bare eyes in distinguishing comma-shaped clouds are *shape* and *motion*. During the formulation of a cyclone, the “head” of the comma-shaped cloud, which is the northern and western cloud shield, has a strong rotation feature. The dense cloud patch forms the shape of a comma, which distinguishes the cloud patch from other clouds. To emulate meteorologists, we propose two novel features that consider shape and motion of the cloud patches, namely, *Segmented HOG* and *Motion Correlation Histogram*, respectively. We will detail our proposals in Sec. III-A and Sec. III-B.

Our work has two main contributions. First, we propose novel shape and motion features of the cloud using computer vision techniques. It enables computers to recognize the comma-shaped cloud from satellite images. Second, we develop an automatic scheme to detect the comma-shaped cloud on the satellite images. Since the comma-shaped cloud is a visual indicator of severe weather events, our scheme can help meteorologists forecast extreme weather events.

A. Related Work

Cloud segmentation is an important method to detect storm cells. Lakshmanan *et al.* [8] proposed a hierarchical cloud texture segmentation method for satellite images, and threshold higher intensity in the image to identify storms. Later, Lakshmanan *et al.* applied the watershed transform to segment the cloud patches and used pixel intensity thresholding to define storms [9]. However, brightness temperature in a single satellite image is easily affected by lighting conditions, geographical location, and satellite imager quality, which is not fully considered in the thresholding based methods. Therefore, we consider these spatial and temporal factors and segment the high cloud part based on the Gaussian Mixture Model (GMM).

Cloud motion estimation is also an important method for storm detection, and a common approach estimates cloud movements through cross-correlation over adjacent images. Some earlier work [10], [11] applied the cross-correlation method to derive the motion vectors from cloud textures, which was later extended in [12] to multi-channel satellite images. The cross-correlation method could partly characterize the airflow dynamics of the atmosphere and provide meaningful speed and direction information on large areas [13]. After being introduced in the radar reflectivity images in [14], the

method was applied in the automatic cloud tracking systems using satellite images [15]. A later work [16] implemented the cross-correlation in predicting the Mesoscale Convective Systems (MCS, a type of storms) and tracking them. Their motion vectors were computed by aggregating nearby pixels at two consecutive frames, thus are subject to spatially smoothed effects and miss fine-grained details. Inspired by the ideas of motion interpretation, we define a novel correlation aiming to recognize cloud motion patterns in a longer period. The combination of motion and shape features demonstrates high accuracy on our manually labeled dataset.

Researchers have applied pattern recognition techniques to interpret the storm formulation and movement extensively. Before the satellite data reached a high resolution, earlier works constructed storm formulation models based on 2D radar reflectivity images in the 1970s. The primary techniques can be categorized into *cross correlation* [14] and *centroid tracking* [17] methods. According to the analysis in [13], cross-correlation based methods are more capable of accurate storm speed estimation, while centroid tracking based methods are better at tracking isolated storm cells.

Taking advantages of these two ideas, Dixon and Wiener developed the renowned centroid-based storm nowcasting algorithm, named Thunderstorm Identification, Tracking, Analysis and Nowcasting (TITAN) [18]. This method consists of two steps: identifying the isolated storm cells and forecasting possible centroid locations. Compared with former methods, TITAN can model and track some storm merging and splitting cases. But this method could have large errors if the cloud shape changes quickly [19]. Some later works attempted to mathematically model the storm identification process. For instance, [20] and [21] used statistical features of the radar reflect to classify regions into storm or stormless classes.

Recently, Kamani *et al.* proposed a severe storm detection method by matching the skeleton feature of bow echoes (*i.e.* visual radar patterns associated with storms) on radar images [22]. The idea is inspiring, but the radar reflectivity images have some weaknesses in extreme weather precipitation [23]. First, the distribution of radar stations in the contiguous United States (CONUS) is uneven. The quality of ground-based radar reflectivity data is affected by the distance to the closest radar station to some extent. Second, detections of marine events cannot reach the accuracy as that on land, because there are no ground stations in the oceans to collect reflectivity signals. Finally, severe weather condition would affect the accuracy of radar. Since our focus is on severe weather event detection, radar information may not provide enough timeliness and accuracy for detection purpose.

Compared with the weather radar, multi-channel geosynchronous satellites have larger spatial coverages, providing more global information to the meteorologists. Take the infrared spectral channel in the satellite imager as an example, the brightness of a pixel reflects the temperature and the height of the cloud top position [24], which in turn provides the physical condition of the cloud patch at a given time. To find storm information, researchers have applied many pattern recognition methods to satellite data interpretation, like combining multiple channels image information of the

weather satellite [12] and combining images from multiple satellites [25]. Image analysis methods, including cloud patch segmentation and background extraction [8] [26], cyclone identification [27] [28], cloud motion estimation [29], and vortex extraction [30], have also been incorporated in severe weather forecasting from satellite data. However, these approaches lack an attention mechanism that can focus on areas most likely to have major destructive weather conditions. Most of these methods do not consider high-level visual patterns to describe the severe weather condition. Instead, they represent extreme weather phenomena by relatively low-level image features.

B. Proposed Spatiotemporal Modeling Approach

In contrast, meteorologists, who have geographical knowledge and rich experience of analyzing past weather events, typically take a top-down approach. They make sense of available weather data in a more global (in contrast to local) fashion than numerical simulation models. For instance, meteorologists can often make reasonable judgments about near-future weather conditions by looking at the general cloud patterns and the developing trends from satellite image sequences, while existing pattern recognition methods in weather forecasting do not capture such high-level clues such as comma-shaped clouds. Unlike the conventional object detection task, detecting comma-shaped clouds is highly challenging. First, some parts of cloud patches can be missing from satellite images. Second, such clouds vary substantially in terms of scales, appearance, and moving trajectory. Standard object detection techniques and their evaluation methods are inappropriate.

To address these issues, we propose a new method to detect the comma-shaped cloud in satellite images. Our framework implemented computer vision techniques to design the task-dependent features, and it includes re-designed data processing pipelines. As a result, we can effectively identify comma-shaped clouds from satellite images. In the evaluation and case study section, we show that our method contributes to storm forecasting using real-world data, and it can produce earlier and more sensitive detections than human perception in some cases.

The remainder of the paper is organized into four sections. Section II describes the satellite image dataset and the training labels. Sec. III provides details on the machine learning framework, with the evaluations in Sec. IV. We provide some case studies in Sec. V and draw a conclusion in Sec. VI.

II. THE DATASET

Our dataset consists of the GOES-M weather satellite images for the year 2008 and the GOES-N weather satellite images for the years 2011 and 2012. These three years are selected because they had more severe thunderstorm activities in the U.S. than a typical year. GOES-M and GOES-N weather satellites are in the geosynchronous orbit of the earth and provide continuous monitoring for intensive data analysis. Among the five channels of the satellite imager, we adopt the fourth channel, because it is infrared among the wavelength range of (10.20 - 11.20 μ m), capturing objects of meteorological interest including clouds and sea surface [31]. The channel is at the

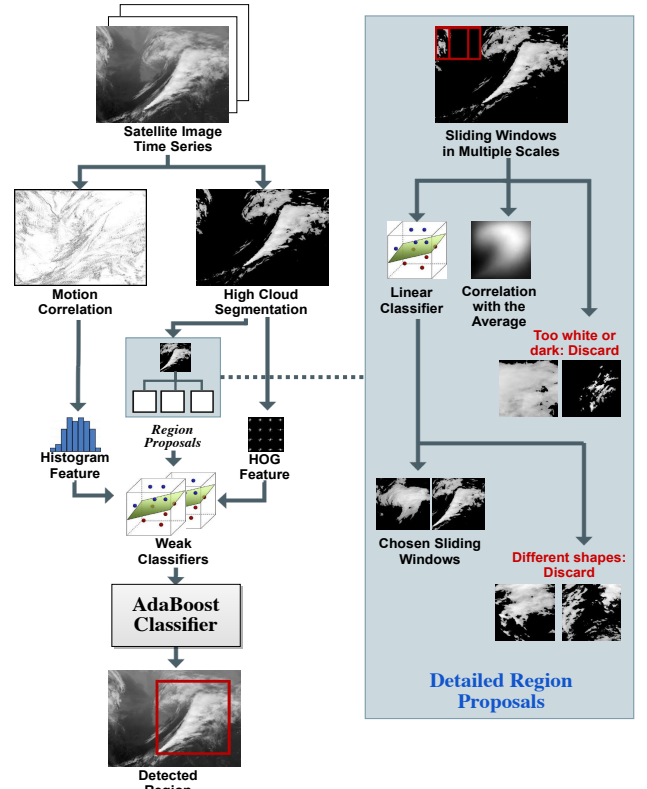


Fig. 2. *Left*: The pipeline of the comma-shaped cloud detection process. high-cloud segmentation, region proposals, correlation with motion prior, constructions of weak classifiers, and the AdaBoost detector are described in Sections III-A, III-B, III-D, III-E, and III-F respectively. *Right*: The detailed selection process for region proposals.

resolution of 2.5 miles and the satellite takes pictures of the northern hemisphere at the 15th minute and the 45th minute of each hour. We use these satellite frames of CONUS at 20°-50° N, 60°-120° W. Each satellite image has 1,024 \times 2,048 pixels, whose gray-scale intensity is positively correlated with the infrared temperature. After the raw data are converted into the image data in accordance with the information in [32], each image pixel represents a specific geospatial location.

The labeled data of this dataset consist of two parts, (1) comma-shaped clouds identified with the help of meteorologists of AccuWeather Inc., and (2) an archive of storm events for these three years in the U.S. [33].

In the first part of the labeled data, we use square bounding boxes to label the areas covered by comma-shaped clouds. If a comma-shaped cloud moves out of the range, we ensure that the head and tail of the comma are in the middle part of the square. The labeled comma-shaped clouds are of a wide range of visual appearances, and their coverage can vary from a width of 70 miles to 1,000 miles. Automatic detection of them is thus nontrivial. The labeled dataset includes a total of 10,892 comma-shaped cloud frames in 9,321 images for the three years 2008, 2011, and 2012. Most of them follow the earlier description of comma-shaped clouds, with the visible rotating head part, main body heading from southwest to northeast, and the dark dry slot area between them.

The second part of the labeled data consists of storm observations with detailed information, including time, locations, range, and types. Each storm is represented by its

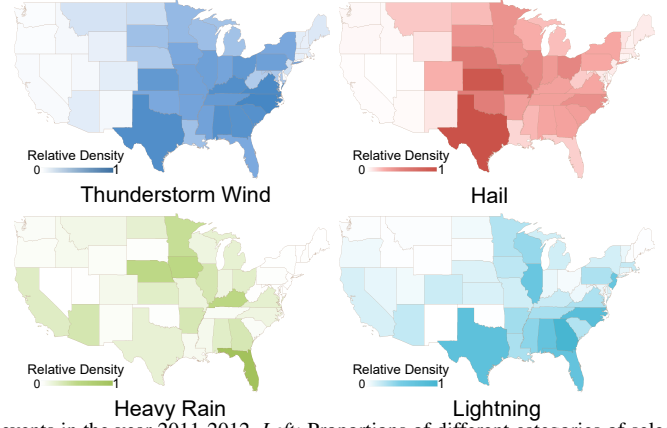
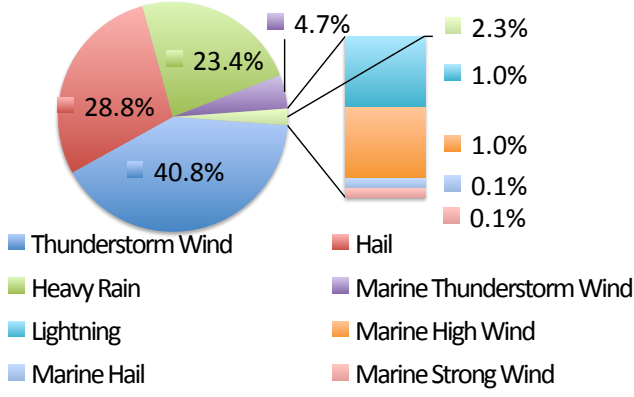


Fig. 3. Proportions and geographical distributions of different severe weather events in the year 2011-2012. *Left*: Proportions of different categories of selected storm types. *Right*: State-wise geographical distributions of land-based storms.

latitude and longitude in the record. We ignore the range differences between storms because the range of storms is relatively small (< 5 miles) compared with our bounding boxes ($70 \sim 1000$ miles) in size. Every event recorded in the database had enough severity to cause loss of life, injuries, significant property damage, and disruption to commerce. The total estimated damage from storm events during 2011-2012 was more than two billion dollars [34]. From the database, we chose eight types of severe weather records¹ that are known to have a strong correlation with the comma-shaped clouds and happen most frequently among all types of events. The distribution of types of severe weather events is shown in the left half of Fig. 3. Among those eight types of severe weather events, thunderstorm winds, hails, and heavy rains happen most frequently ($\sim 93\%$ of the total). The state-wise geographical distributions of some types of storm events are in the right half of Fig. 3. Because marine-based events don't have their associated state information, we only visualize the geographical distributions for land-based storm events. These severe weather events happen more frequently in East CONUS except for heavy rains.

In our experiments, only storm records that lasted for more than 30 minutes are kept for further evaluation, because they overlap with at least one satellite image in the dataset. Consequently, we have 5,412 severe storm records for the year 2011 and 2012 in the CONUS area for testing purpose, and their last time varies from 30 minutes to 28 days.

III. OUR PROPOSED DETECTION METHOD

Fig. 2 shows our proposed comma-based cloud detection pipeline framework. We first segment cloud from the background in Sec. III-A, then we extract shape and motion features of clouds in Sec. III-B. Well-designed region proposals in Sec. III-D help shrink the searching range on satellite images. The features on our extracted region proposals are fed into weak classifiers in Sec. III-E and then we ensemble these weak classifiers as our comma-shaped cloud detector in Sec. III-F. We now detail the technical setups in this section.

A. high-cloud segmentation

We first segment the high cloud part out from the noisy original satellite data. Raw satellite images contain all the

objects that can be seen from the geosynchronous orbit, including land, seas, and clouds. Among all the visible objects in satellite images, we focus on the dense middle and top cloud, which we refer to as “high cloud” in the following. The high cloud is important because the comma-shaped phase is most evident in this part, according to [4].

The prior work [35] implemented the single-threshold segmentation method to separate cloud from the background. This method is based on the fact that high cloud looks brighter than other parts of the infrared satellite images [24]. We evaluate this method and show the result in the second column of Fig. 4. Although this method can segment most high cloud out from the background, it misses some cloud boundaries. Because the earth has periodic temperature changes and ground-level temperature variations, which vary with terrains, elevation, and latitudes, a single threshold cannot adapt to all these cases.

The imperfection of the prior segmentation method motivates us to opt this single threshold segment scheme and explore a data driven approach. The overall idea of the new segmentation scheme is described as follows: To be aware of spatiotemporal changes of the satellite images, we divide the image pixels into tiles, and then model the samples of each unit using a GMM. Afterward, we identify the existence of a component that most likely corresponds to the variations of high cloudy-sky brightness.

We build independent GMMs for each month and each spatial region for the concern of periodical sunlight changes and terrain affections. Suppose all pixels are indexed by their time stamp t and spatial location \mathbf{x} , we divide each day into 24 hours, and divide each image into non-overlapping windows. Each window is a square of 32×32 . Thus, for each hour h and each window L , i.e. $T_h \times X_L$, we form a group of pixels $G_{h,L} = \{I(t, \mathbf{x}) : t \in T_h, \mathbf{x} \in X_L\} = \{I_{h,L}(t, \mathbf{x})\}$, with brightnesses $I(t, \mathbf{x}) \in [0, 255]$. Roughly, each pixel group $G_{h,L}$ has 150,000 samples. We model each group by a GMM with the number of components of that group $K_{h,L}$ to be 2 or 3, i.e.:

$$I_{h,L}(t, \mathbf{x}) \sim \sum_{i=1}^{K_{h,L}} \varphi_{h,L}^{(i)} \mathcal{N} \left(\mu_{h,L}^{(i)}, \Sigma_{h,L}^{(i)} \right),$$

where

$$K_{h,L} = \arg \min_{i=2,3; (t, \mathbf{x}) \in T_h \times X_L} \{AIC(K_{h,L} = i | t, \mathbf{x})\}.$$

¹Tornadoes are included in the Thunderstorm Wind type.

Here $AIC(\cdot)$ is the Akaike information criterion function of $K_{h,L}$. $\psi_{h,L} = \left\{ \varphi_{h,L}^{(i)}, \mu_{h,L}^{(i)}, \Sigma_{h,L}^{(i)} \right\}_{i=1}^{K_{h,L}}$ are GMM parameters satisfying $\mu_{h,L}^{(i)} > \mu_{h,L}^{(j)}$ for $\forall i > j$, which are estimated by k-means++ method. We can interpret the GMM component number $K = 2$ as the GMM peaks fit high-sky cloud and land, while $K = 3$ as the GMM peaks fit high-sky cloud, low-sky cloud, and the land. So for each GMM $\psi_{h,L}$, the component with the largest mean is the one modeling high cloudy-sky. We then compute the normalized density of the point (t, \mathbf{x}) over $\psi_{h,L}$. We annotate this normalized density as $\left\{ p_{h,L}^{(i)}(t, \mathbf{x}) \right\}_{i=1}^{K_{h,L}}$ and define the intensity value after segmentation to be: $\tilde{I}(t, \mathbf{x}) :=$

$$\begin{cases} I_{h,L}(t, \mathbf{x}) \cdot p_{h,L}^{(1)}(t, \mathbf{x}) & \text{if } I_{h,L}(t, \mathbf{x}) \cdot p_{h,L}^{(1)}(t, \mathbf{x}) \geq \sigma \\ 0 & \text{otherwise,} \end{cases} \quad (1)$$

where σ is chosen empirically between 100 and 130, with low impact to the features extracted. In our experiment, we choose 120 for convenience.

We then apply a min-max filter between neighbouring GMMs in spatiotemporal space. Based on the assumption that cloud movement is smooth in spatiotemporal space, GMM parameters $\psi_{h,L}$ should be a continuous function over h and L . For most pixel groups which we have examined, we observe that our segmented cloud changes smoothly. But in case GMM component number changes, $\mu_{h,L}^{(1)}$ would have a big change in both h and L , resulting in the segmented cloud changes significantly. To smooth the cloud boundary part, we post-process a min-max filter to update $\mu_{h,L}^{(1)}$, which is given by

$$\mu_{h,L}^{(1),\text{new}} := \max \left\{ \mu_{h,L}^{(1)}, \min_{\substack{h' \in \mathcal{N}_h \\ L' \in \mathcal{M}_L}} \{ \mu_{h',L'}^{(1)} \} \right\}, \quad (2)$$

where \mathcal{N}_h is the neighboring hours of h , and \mathcal{M}_L is the spatial neighboring windows of L . The min-max filter leverages smoothness of GMMs within spatiotemporal neighbours. After filtering with Eq. 2, we update normalized densities and get more smooth results with Eq. 1. Example high-cloud segmentation results are shown in the third column of Fig. 4. At the end of this step, high clouds are separated with detailed local information, while the shallow clouds and the land are removed.

B. Correlation with Motion Prior

Another evident feature of the comma-shaped cloud is motion. In the cyclonic system, the jet stream has a strong trend to rotate around the low center, which makes up the head part of the comma in the satellite image [17]. We design a visual feature to extract this cloud motion information, namely *Motion Correlation* in this section. The key idea is that the *same* cloud at two *different* spatiotemporal points should have a strong positive correlation in appearance, based on a reasonable assumption that clouds move at a nearly-uniform speed within a small spatial and time span. Thus, cloud movement direction can be inferred from the direction of the maximum correlation. This assumption was first applied to compute cross-correlation in [10].

We therefore define the motion correlation of location \mathbf{x} on the time interval of $(t - T, t]$ to be:

$$M(t, \mathbf{x}) = \text{corr}_{t_0 \in (t-T, t]}(I(t - t_0, \mathbf{x}), I(t, \mathbf{x} + \mathbf{h})), \quad (3)$$

where $\text{corr}(\cdot, \cdot)$ denotes the Pearson correlation coefficient, and \mathbf{h} is the cloud displacement distance in time interval T . This motion correlation can be viewed as an improved cross-correlation in [10], which we mentioned in Sec. I. The cross-correlation can be written as the following form:

$$M_0(t, \mathbf{x}) = \text{corr}_{\|\mathbf{x}_1 - \mathbf{x}\| \leq h_0}(I(t - T_0, \mathbf{x}), I(t, \mathbf{x}_1 + \mathbf{h})), \quad (4)$$

where T_0 is the time span between two successive satellite images.

We can conclude that our motion correlation is *temporally smoothed* and the cross-correlation is *spatially smoothed* by comparing Eq. 3 and 4. The cross-correlation feature focuses on the differences in only two images, and then takes the average on a spatial range. On the other hand, our correlation feature, with motion prior, interprets movement accumulation during the whole time span. We further re-normalize both $M(\cdot, \cdot)$ and $M_0(\cdot, \cdot)$ to $[0, 255]$ and visualize these two motion descriptors in the fourth and fifth columns of Fig. 4, where we fix $\mathbf{h} = 10$ pixels, $T = 5$ hours and $h_0 = 128$ pixels. The cross-correlation feature (fourth column of Fig. 4) is noncontinuous across the area boundary. In image time series, cross-correlation feature expresses less consistent positive/negative correlation in one neighboring than our motion correlation. Compared with the cross-correlation feature, our motion correlation feature (fifth column of Fig. 4) shows more consistent texture paralleled to the cloud motion direction.

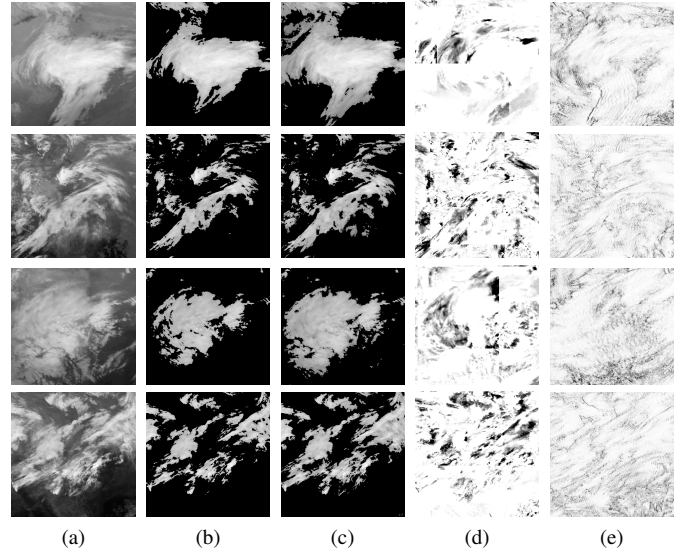


Fig. 4. Cropped satellite images. (a) The original data. (b) Segmented high cloud with single threshold. (c) Segmented high cloud with GMM. (d) Cross-correlation in [10]. (e) Correlation with motion prior.

C. Data Partition

In this section, we use the widely-used “sliding windows” in [36] as the first-step detection. Sliding windows with an image pyramid help us capture the comma-shaped cloud at various scales and locations. Because we only consider the comma-shaped cloud in the high-sky, we run our sliding windows on the segmented cloud images. We set 21 dense sliding window sizes at $L \times L$ pixels, where $L \in$

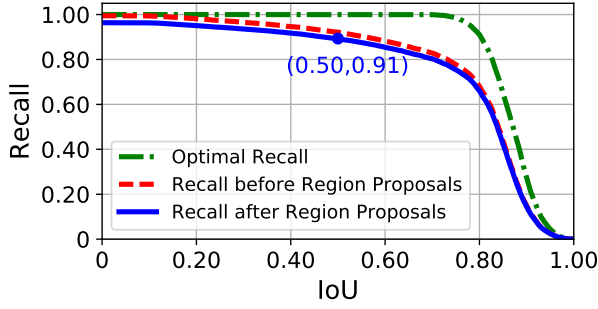


Fig. 5. IoU-Recall curve in the Region Proposal steps. The blue dot on the blue curve is our final IoU choice, with the corresponding recall of 0.91 .

$\{128, 128 \cdot 8^{1/20}, \dots, 128 \cdot 8^{19/20}, 1024\}$. For each sliding window size L , the movement pace of the sliding window is $\lfloor L/8 \rfloor$, where $\lfloor \cdot \rfloor$ indicates the floor function. Under that setting, each satellite image has more than 10^4 sliding windows, which is enough to cover the comma-shaped cloud in different scales.

It is important to define a given bounding box is positive or negative before we apply some machine learning techniques. Here we use the Intersection over Union metric (IoU) [37] to design the positive and negative samples, which is also a common criterion in object detections. We set bounding boxes with IoU larger than a value to be the positive examples, and those with IoU = 0 to be the negative samples.

A suitable IoU threshold should ensure region proposals to have both reasonable high recall rate and visual similarity with comma-shaped clouds. We cannot achieve near-perfect recall rate in our case because of several factors. First, we only choose limited sizes of sliding windows with limited strides. Second, some of the satellite images are (partially) corrupted and unsuitable for a data-driven approach. Third, some cloud patches are in a lower altitude, hence they are removed in the high-cloud segmentation process in Sec. III-A. Fourth, we design simple classifiers to filter out most sliding windows without comma-shaped clouds (see Sec. III-D). Though we can get high efficiency by region proposals, we filter a small portion of true comma-shaped clouds. We show the IoU-recall curves in Fig. 5 for analyzing the effect of these factors to the recall rate. We provide our choice of IoU as the blue dot in the plot and explain the reasons below.

Among the three curves in Fig. 5, the green curve, marked as the *Optimal Recall*, indicates the theoretical highest recall rate we can obtain with IoU changes. Because we have strong requirements to the sizes and locations of sliding windows in our algorithm, but we do not assert those restrictions to human labelers, labeled regions and sliding windows cannot have a 100% overlap due to human perception variations. Thus, we use the maximum IoU between each labeled region and all sliding windows as the highest theoretical IoU of this algorithm. The red curve, marked as *Recall before Region Proposals*, indicates the true recall we can get which considers missing images, image corruption, and high-cloud segmentation errors. Within our dataset, there are 11.26% (5,926) of satellite images that are missing from the NOAA satellite image dataset, 0.36% (188) that no clouds were recognized, and 3.33% (1,751) that have abnormally low contrast. Though low contrast level or dark images can be adjusted by histogram

equalization, the Gaussian distributions in the background extraction step are disturbed. Some high clouds are mistakenly removed with the background as a result. In that experimental setting, this curve is the highest recall we can get before region proposals. The blue curve, marked as *Recall after Region Proposals*, indicates the true recall we can get after region proposals, where the detailed process to design region proposals is in the following (Sec. III-D).

The positive training samples consist of sliding windows whose IoU with labeled regions are higher than a threshold. This threshold value is carefully chosen to guarantee both a reasonably high recall and a high accuracy. As a convention in object detection tasks, we expect IoU threshold ≥ 0.50 to ensure visual similarity with manually labeled comma-shaped clouds, and a reasonable high recall rate ($\geq 90\%$) in total for enough training samples. Finally, the IoU threshold is set to be 0.50 for our task. The recall rate is 92.26% before region proposals and 90.66% after region proposals.

Then we partition the dataset into three parts: *training set*, *cross-validation set*, and *testing set*. We use the data of the first 250 days of the year 2008 as the training set, the last 116 days of that year as the cross-validation set, and data from the years 2011 and 2012 are used as the testing set. This separation is due to a large number of the severe storms in 2008, and the storm distribution ratio in the training, cross-validation, and testing set are roughly 50% : 15% : 35%. There are strong data dependencies between consecutive images. Splitting our data by time rather than randomly, breaking this type of dependencies, more realistically emulates the scenario when our system is applied. This data partitioning scheme is also valid in the following.

D. Region Proposals

In this stage, we design some simple classifiers to filter out a majority of negative sliding windows. This method was also applied in [38]. Because only a very small proportion of sliding windows generated in Sec. III-C contain comma-shaped clouds, we can save computation on further training and testing processes by reducing the amount of sliding windows.

We apply three weak classifiers to decrease the number of sliding windows. The first classifier removes candidate sliding windows if their average pixel intensity is out of range [50, 200]. As stated before, comma-shaped clouds have typical shape characteristics that its cloud body consists dense cloud and the dry tongue area is cloudless. Hence, the average intensity of a well-cropped cloud patch should be within a certain range, neither too bright nor too dark. Finally, this classifier removes most cloudless bounding boxes while keeping over 98% of the positive samples.

The second classifier uses a linear margin to separate positive examples from negative ones. We train this linear classifier on all the positive sliding windows with an equal number of randomly chosen negative examples, and then validate on the cross-validation set. All the sliding windows are resized to 256×256 pixels and vectorized before fed into training, and the response variable is positive (1) or negative (0). As a result, the classifier has an accuracy over 95% on the training

set and over 80% on the cross-validation set. To ensure the recall of our detectors, we output probability of each sliding window, and then set a low threshold value. Sliding windows that output probability less than this threshold value are filtered out and we should ensure no positive samples are filtered. We randomly change the train-test split for ten rounds and set the final threshold value to be 0.2.

Finally, we calculate the pixel-wise correlation γ of each sliding window I with the average comma-shaped cloud I_0 . This correlation captures the similarity to a comma shape. γ is computed as:

$$\gamma = \frac{I \cdot I_0}{\|I\|_{L_2} \cdot \|I_0\|_{L_2}}. \quad (5)$$

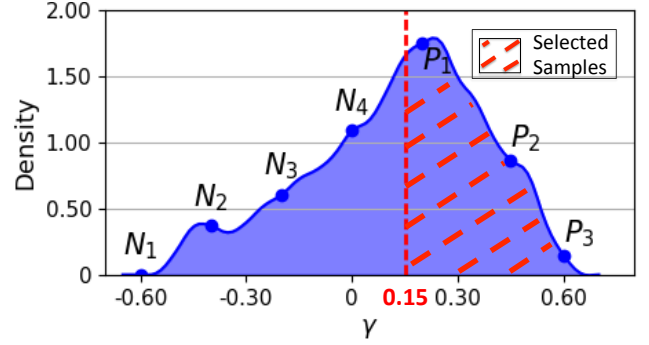
Here I_0 represents a reference of the comma shape. Because there are no evident visual differences between different categories of storms (as shown in the last row of the table in Fig. 6), and some comma-shaped clouds do not lead to future storms, I_0 is averaged using all the labeled comma-shaped cloud in the training set. The computation process of I_0 consists of the following steps. First, we take all the labeled comma-shaped cloud bounding boxes in the training set, resizing them to 256×256 . Next, we segment the high-cloud part from each image. Finally, we take the average of the high-cloud parts. The resulting I_0 is marked as Avg. in the middle row of the table in Fig. 6. To be consistent in dimensions, every sliding window I is also resized to 256×256 in Eq. 5.

The higher correlation γ indicates that a cloud has the appearance of a comma-shaped cloud. Based on this observation, a simple classifier is designed to select sliding windows whose γ is higher than a certain threshold. Fig. 6 serves as a reference to choose a customized threshold of γ , where we provide the distribution and some example images of γ in the table of Fig. 6. In the training and cross-validation sets, less than 1% of positive examples have a γ value lower than 0.15. So we use $\gamma \geq 0.15$ as the final filter choice to eliminate sliding window candidates.

As a result, the region proposal process only let pass about 10^3 bounding boxes per image, which is only one tenth of the initial number of bounding boxes. As shown in Fig. 5, the region proposals do not significantly affect the recall rate, but much computational time is saved through this process.

E. Construction of Weak Classifiers

We construct two sets of features for describing each of the proposed regions, in order to correctly detect comma-shaped clouds among all region proposals separated from the satellite images. The first is the histogram of oriented gradients (HOG)[38] feature based on segmented high clouds. For each of the region proposal, we calculate the HOG feature of the bounding box. Because we compute HOG feature on the segmented high cloud, we refer it *Segmented HOG* feature in the following paragraphs. The second is the histogram feature of each image crop based on the motion prior image, where the texture of the image reflects the motion information of cloud patches. We fine-tune the parameters and show the accuracy on cross-validation set in Table I. We use Segmented HOG setting



Marker	N_1	N_2	N_3	N_4
γ	-0.60	-0.40	-0.20	0
Example				
Marker	P_1	P_2	P_3	—
γ	0.20	0.40	0.60	Avg.
Example				
TS.* Category	TS. Wind	Lightning	Hail	Marine TS.Wind
Avg. Image				

* TS.: Thunderstorm.

Fig. 6. Top: The correlation probability distribution of all sliding windows. Middle: Some segmented image examples. The last example image is the average image of the manually labeled regions in the training set. The correlation score γ is defined in Eq. 5, and the diagram is the normalized probability distribution of γ of the training set. Bottom: Average comma-shaped cloud in different categories.

TABLE I
AVG. ACCURACY OF WEAK CLASSIFIERS FOR THE SEGMENTED HOG AND MOTION HISTOGRAM FEATURES IN DIFFERENT PARAMETER SETTINGS

Seg. HOG Settings	Orientation Directions	Pixels/Cell	Cells/Block	(%)Avg. Accuracy
#1	9	64×64	1×1	69.88 ± 1.15
#2	18	64×64	1×1	70.65 ± 1.25
#3	9	128×128	1×1	61.21 ± 0.62
#4	9	64×64	2×2	73.18 ± 0.98
Motion Hist. Settings	Pixels to the West h^*	Time Span in hours T^*	Hist. Bins	(%)Avg. Accuracy
#1	10	2	18	58.84 ± 0.59
#2	5	2	18	52.97 ± 0.20
#3	10	2	9	58.83 ± 0.20
#4	10	2	27	61.05 ± 0.63
#5	10	5	27	63.25 ± 0.67

* h and T have the same meaning as annotated in Eq. 3.

#4 and Motion Histogram Setting #5 as the final choice in our experiments because this setting has a better performance on the cross-validation set. The feature dimension is 324 for Segmented HOG and 27 for Motion Histogram.

Since severe weather events have a low frequency to happen, positive examples only take up a very small proportion ($\sim 1\%$) in the whole training set. To fully utilize negative samples in the training set, we construct 100 linear classifiers. Each of these classifiers is trained on the whole positive training

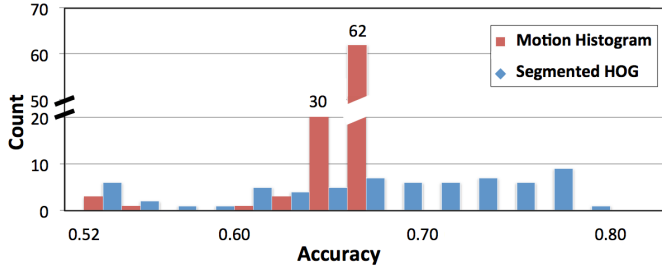


Fig. 7. The accuracy distribution of weak classifiers with Segmented HOG feature and Motion Histogram feature.

set and an equal number of negative samples. We split and randomly select these 100 batches according to their time stamp so that their time stamps are not overlapped with other batches. We train a logistic regression on the segmented HOG features and the motion histogram feature of the training set. Finally, we get 200 linear classifiers. We evaluate the accuracy of the trained linear classifiers based on a subset of testing examples whose positive/negative ratio is also 1-vs-1. The average accuracy of the segmented HOG feature is 73.18% and that of the motion histogram features is 63.25%. The accuracy distribution of these two types of weak classifiers is shown in Fig. 7. From the statistics and the figure, we know Segmented HOG feature has a higher average accuracy than that of Motion Histogram feature, and also a larger variation in the accuracy distribution. As shown in Fig. 7, about 90% of the classifiers on motion histogram feature have an accuracy between 63% to 65%, while those on segmented HOG feature distribute in a wide range from 53% to 80%.

F. AdaBoost Detector

We apply the stacked generalization on the probability output of our weak classifiers [39]. For each proposed region, we use the probability output of the 200 weak classifiers as an input, and then get one probability p as an output. We define the proposed region is positive for $p \geq p_0$ or negative in other cases, where $p_0 \in (0, 1)$ is our given cutoff value.

We adopt AdaBoost method [40] as the method for stacked generalization because it reaches the highest accuracy on the balanced cross-validation set, as shown in Table II. All these classifiers are constructed on the training set and fine-tuned on the cross-validation set. Table III-F shows the accuracy of the AdaBoost classifier reaches the maximum at 86.47% with 40 leaf nodes and one layer. As a result, The AdaBoost classifier running on region proposals is our proposed comma-shaped cloud detector.

In our experiment, the training set for ensembling is a combination of all 68,708 positive examples and a re-sampled subset of negative examples sized 10 times larger than the size of positive examples (*i.e.*, 687,080). We carry out experiments with the Python 2.7 implementation on a server with the Intel® Xeon X5550 2.67GHz CPUs. The minimum parallel model is one satellite image. If the cutoff threshold is set to be 0.50, the detection process for one image, from high-cloud segmentation to AdaBoost detector, costs about 40.59 seconds per image. Within that time, the high-cloud segmentation takes 4.69 seconds, region proposals 14.28 seconds, and the

TABLE II
ACCURACY OF DIFFERENT STACKED
GENERALIZATION METHODS ON
THE CROSS-VALIDATION SET

Method*	(%)Accuracy
LR	85.12
Bagging	81.98
RF	82.35
ERF	82.37
GBM	86.23
AdaBoost	86.47

* LR: Logistic Regression;
RF: Random Forest; ERF:
Extremely Random Forest;
GBM: Gradient Boosting
Machine with deviance loss.

TABLE III
ACCURACY OF THE ADABOOST
DETECTOR ON THE
CROSS-VALIDATION SET WITH
DIFFERENT PARAMETERS

Tree layer	Leaf Nodes	(%)Accuracy
1	20	85.49
	40	86.47
	60	86.45
2	20	86.11
	40	86.27
	60	84.97

TABLE IV
ACCURACY OF THE ADABOOST CLASSIFIER ON THE CROSS-VALIDATION
SET WITH DIFFERENT FEATURES

With high-cloud segmentation	Feature(s)	Accuracy (%)
No	HOG	70.49
	Motion Hist.	55.96
	Combination	80.33
Yes	HOG	73.68
	Motion Hist.	65.50
	Combination	86.47

Here HOG with high-cloud segmentation = Segmented HOG feature; Motion Hist. = Motion Histogram Feature.

AdaBoost detector 21.62 seconds. We only get two satellite images per hour now, and these three processes finish in a sequential order. If higher speed is in need, an implementation in C/C++ is expected to be substantially faster.

We then run our AdaBoost detector on our testing set and then calculate the ratio of the labeled comma-shaped cloud that our method can detect. Within each image, we choose the detection regions that have the largest probability scores of having comma-shaped cloud (abbr. as probability in this paragraph), and we ensure every two detection regions in one image have an IoU less than 0.30 — a technique called non-maximum suppression (NMS) in object detection [41]. If one output region has IoU larger than 0.30 with another output region, we remove the one with lower probability from the AdaBoost detector. Finally, the detector outputs a set of sliding windows, with each region indicating one possible comma-shaped cloud.

IV. EVALUATION

In this section, we present the evaluation results for our detection method. First, we present an ablation study. Second, we show that our method can effectively detect both comma-shaped clouds and severe thunderstorms. Finally, we compare our method with two other satellite-based storm detection schemes and show that our method outperforms them.

A. Ablation Study

To examine how much each step contributes to the model, we carried out an ablation study and show the results in Table IV. In this table, we enumerate all the combinations in terms of high-cloud segmentations and features. The first column indicates whether the region proposals are on the

original satellite images or on the segmented ones. The second column separates HOG feature, Motion Histogram feature, and their combinations. The last column shows the accuracy on the cross-validation set. If we do not use high-cloud segmentation, the combination of HOG and Motion Histogram features outperforms each of them. If we use high-cloud segmentation, the combination of these two features also performs better than each of them, and it also outperforms the combination of features without high-cloud segmentation. In conclusion, the effectiveness of our detection scheme is due to *both* high-cloud segmentation process and weak classifiers built on shape and motion features.

B. Detection Result

The evaluation in Fig. 8 shows our model can detect up to 99.39% of the labeled comma-shaped cloud and up to 79.41% of storms of the year 2011 and 2012. Here we define the term “detect a comma-shaped cloud” as: if our method outputs a bounding box having $\text{IoU} \geq 0.50$ with the labeled region, we consider such bounding box detects the comma-shaped cloud; otherwise not. We also define “detect a storm” as: if any storm in the NOAA storm database is captured within one of our output bounding boxes, we consider we detect this storm.

Our comma-shaped cloud detector outputs the probability p of each bounding box from AdaBoost classifier. If $p \geq p_0$, we think this bounding box consists comma-shaped cloud. We recommend p_0 to be set in $[0.50, 0.52]$, and we provide three reference points $p_0 = 0.50, 0.51$ and 0.52 . The number of detections per image, the missing rate of comma-shaped cloud and storms corresponding to each p_0 are available in the right part of Fig. 8. For a user who wants high recall rate, like a meteorologist, we recommend setting $p_0 = 0.50$. The recall rate of the comma-shaped cloud is 99% and the recall rate of storms is 64% under that setting. An overhead is that, our detection method will output an average of 7.76 bounding boxes per satellite image. Other environmental data, like wind speed and pressure, are needed to cooperate into the system to filter the bounding boxes. On the other hand, for a user who wants accurate detections, we recommend setting $p_0 = 0.52$. The recall rate of the comma-shaped cloud is 80%, and our detector outputs an average of 1.09 bounding boxes per satellite image. The recall rate is reasonable, and the user will not get many false negative samples on each image.

The setting $p_0 \in [0.50, 0.52]$ could give us best performance because of the following reasons. When p_0 goes under the value 0.50, the missing rate of the comma-shaped cloud almost remain the same value ($\sim 1\%$), and we need to check more than 8 bounding boxes per image to find these missing comma-shaped cloud. It consumes too much human effort. When p_0 goes over the value 0.52, the missing rate of comma-shaped cloud goes over 20%, and the missing rate of storms goes over 77%. Since missing a storm could cause severe loss, $p_0 > 0.52$ cannot provide us a recall rate that high enough for the storm detection purpose.

Though our comma-shaped cloud detector can effectively cover most labeled comma-shaped cloud, it still misses at least 20% storms in the record. Among different type of the storms,

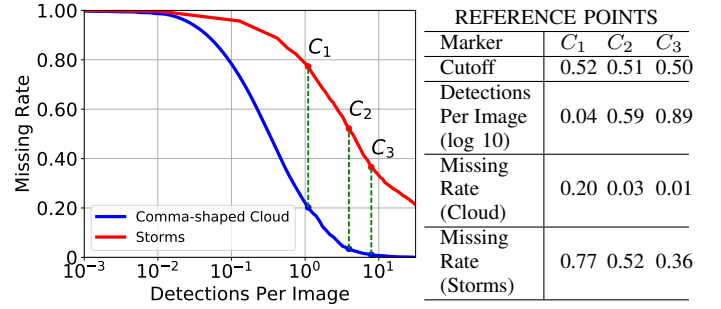


Fig. 8. Evaluation curves of our comma-shaped cloud detection method. Left: Missing rate curve with Detections. Right: Some reference cutoff values on the curve.

severe weather events on the ocean² have a higher probability to be detected in the algorithm than other types of severe weather events. At the point of the largest recall, our method detects approximately 85% severe weather events on the ocean versus 75% on the land. The reason our detector misses them is that, severe weather does not always happen near the low center of the comma-shaped cloud. According to [4] and [42], the exact cold front and the warm front streamline cannot be accurately measured from satellite images. Hence, the comma-shaped cloud is just an indicator of storms, and further investigation in their geological relationships is necessary to improve our method.

C. Storm Detection Ability

We compare the storm identification ability of our algorithm with other baseline methods that use satellite images. The first baseline method comes from [43] and [44], and the second baseline improves the first one in [8]. We call them *Intensity Threshold Detection* and *Spatial-Intensity Threshold Detection* in the following.

The Intensity Threshold Detection uses a fixed reflectivity level of radar or infrared satellite data to identify a storm. A continuous region with a reflectivity level larger than a certain threshold I_0 is defined as a storm attacked area. Spatial-Intensity Threshold Detection improves it by changing the cost function to be a weighted sum:

$$E = \sum_{i=1}^n \lambda d_m(x) + (1 - \lambda) d_c(x),$$

where x is a pixel in the image representing cloud patches, d_m is the spatial distance within the cluster, and d_c is the intensity difference between x and the average of the cluster x is in. It is an iterative process until the cost converges.

We make some necessary changes to the baselines to make our method comparable. First, we explore different I_0 values, because we use the different channels and satellites with the baselines. In addition, the light distribution of images is changed through histogram equalization in the preprocessing stage, so we cannot simply adopt I_0 used in the baselines. Second, we change the irregular detected regions to the square bounding boxes, and use the same criteria to define positive and negative detections. We adopt the idea in [9] and view

²Here severe weather events on the ocean includes marine thunderstorm wind, marine high wind, and marine strong wind.

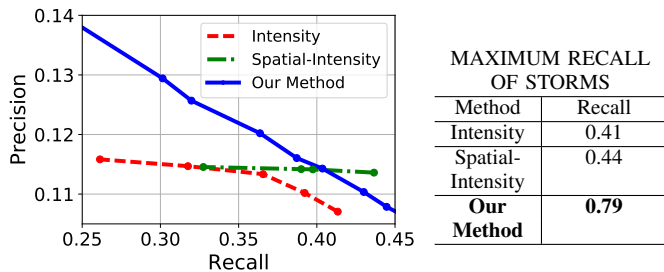


Fig. 9. Comparison of the baseline methods. *Left*: Part of Recall-Precision curve of the two baseline storm detection methods and our method. *Right*: The maximum recall rate they can reach. Here Intensity = Intensity Threshold Detection and Spatial-Intensity = Spatial-Intensity Threshold Detection.

these pixel distributions as 2D GMM. We use Gaussian means and the larger eigenvalue of Gaussian covariance to approximate a bounding box center and a bounding box size, respectively. The number of Gaussian components and other GMM parameters are estimated by mean Silhouette Coefficient [45] and k-means++.

The partial recall-precision curve in Fig. 9 shows our method outperforms Intensity Threshold Detection and it outperforms Spatial-Intensity Threshold Detection when the recall is less than 0.40. We provide only a partial recall-precision curve because of the limited range of I_0 under the limited time and computation resources. In our experiment, we change parameters I_0 in Intensity Threshold Detection from 210 to 230. when I_0 goes over 230, very few pixels would be selected so this method cannot ensure high recall rate. When I_0 goes under 210, many pixels representing low cloud are also included in the computation, which slows down the computations (~ 5 minutes per image). So we do not explore those values. As for Spatial-Intensity Threshold Detection, I_0 is fixed at the value of 225, and λ is the weight between 0 and 1. When λ changes from 0 to 1, the recall first goes up and then moves down, while the precision does not change a lot. The curve representing Spatial-Intensity Threshold Detection reaches the highest recall at 43.66% when λ approaches 0.7.

Compared with two baselines that detect storm events directly, our proposed method has the following strengths. (1) Our method can reach a maximum recall of 79.41%, almost twice as those of the baseline methods. Due to computational speed issues, we could not increase the recall rate of the two baseline methods to be higher than 45%, which limits their use in practical storm detections. But for our method, we can reach a high recall rate without heavy computational cost. (2) Our method outperforms two baseline methods in the precision rate for the most part of Fig. 9. Compared with these two methods that mostly rely on pixel-wise intensity, our method comprehensively combines the shape and motion information of clouds in the system, leading to a better performance in storm detection.

None of the three curves shown in Fig. 9 have a high precision of detecting storm events, because this task is difficult especially without the help of other environmental data. In addition, our method aims to detect comma-shaped clouds, rather than directly forecast storm locations. Sometimes severe storms are reported later than the appearance of comma-shaped clouds. Such cases are not counted in the precision rate of Fig. 9. In those cases, our method can provide useful and

timely information to forecasting meteorologists.

Fig. 9 also points out the importance to explore the spatial relationship between comma-shaped clouds and storm observations, as the Spatial-Intensity Threshold Detection method slightly outperforms our method when the recall rate is higher than 0.40. According to the trend of the green curve, adding spatial information to the detection system can improve the performance to some extent. We will consider combining spatial information into our detection framework in the future.

V. CASE STUDIES

We present three case studies (a-c) in Fig. 10 to show the effectiveness and some imperfections of our proposed detection algorithm. The green bounding boxes are our detection outputs, the blue bounding boxes are labeled comma-shaped cloud, and the red dots indicate severe weather events in the database [33]. The detection threshold is set to 0.52 to ensure the precision of each output bounding box. The descriptions of these storms are summarized from [34].

In the first case (row 1), strong wind, hail and thunderstorm wind developed in the central and northeast part of Colorado state, west of Nebraska and east of Wyoming on late June 06, 2012. The green bounding box in the left-up of (a_1) in the Fig. 10 indicated this region. Then, this dense cloud patch moved in the eastern direction, and covered eastern Wyoming, western South Dakota, and western Nebraska in the early day June 07, 2012. At that time, these states reported property damages in different degrees. In the later time of June 07, 2012, the cloud patch became thinner when moving northward to Montana and North Dakota, as shown in (a_3). Our method had a good tracking of that cloud patch all the time, even though the cloud shape did not look like a typical comma. In comparison, human eyes did not recognize it as a typical comma shape because it lost the head part.

Another region detected to have a comma-shaped cloud in (a_1) was around North Texas and Oklahoma. At that time, hails and thunderstorm winds were reported, but the comma shape in the cloud began to disappear. Another comma-shaped cloud began to form in the Gulf of Mexico, which was in the center part of (a_1). At that time, the comma shape was too vague to be discovered by both our computer detector and by human eyes. As time goes to (a_2), the comma shape had already formulated, and it was detected by both our detector and human eyes. The cloud gathered as some severe events happened in North Florida in (a_2). According to the record, a person got injured and Florida got severe property damages at that time. Later in that day, the large comma-shaped cloud was separated into two part. The cloud patch in the west had an incomplete shape, which is hard for human eyes to discover, as shown in (a_3). However, our method successfully caught this change. In addition, our method caught all the recorded severe weather events. This example indicates our method can detect incomplete or untypical comma-shaped cloud, and it can handle the case that one comma-shaped cloud splits into two parts.

In the second case (row 2), a comma-shaped cloud formulated in the sky over Oklahoma, Kansas, and Missouri on Feb 24, 2011, when these areas were attacked by winter

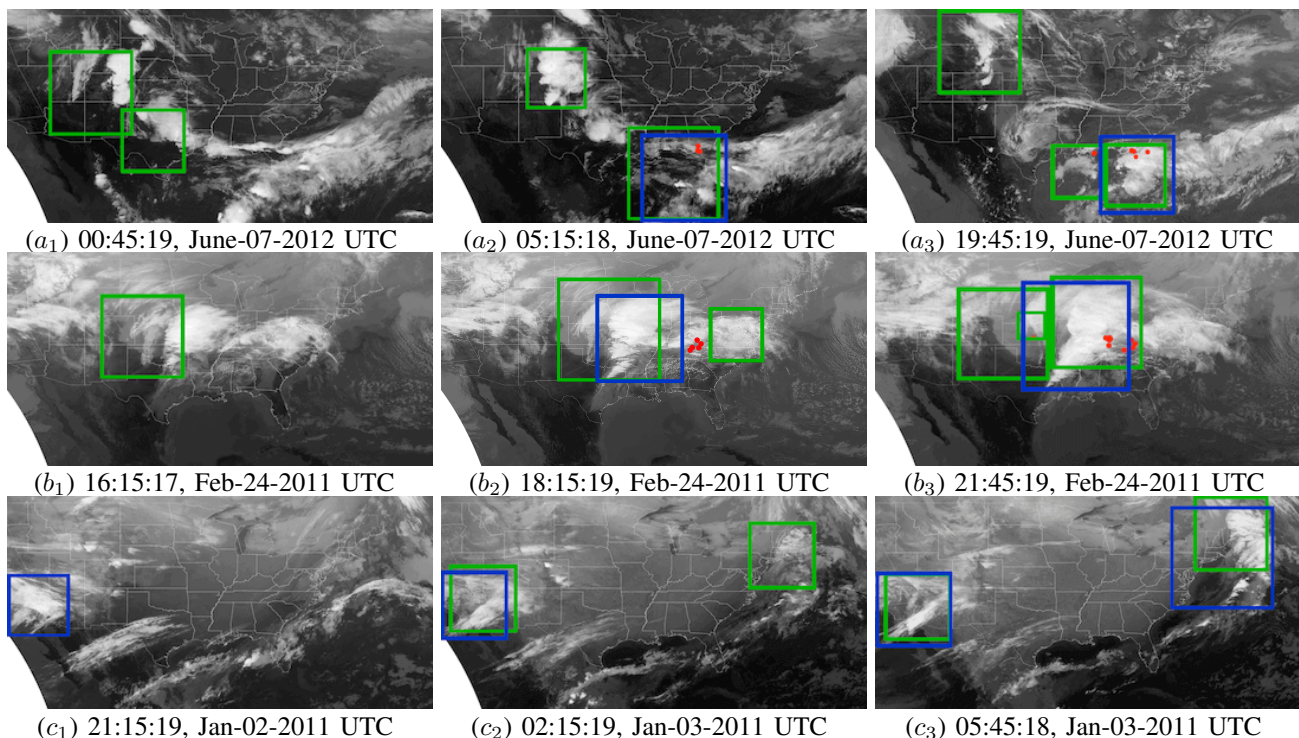


Fig. 10. (a-c) Three detection cases. Green frames: our detection windows; Blue frames: our labeled windows; Red dots: storms. Some images have blank in left-bottom because it is out of the satellite range.

weather, flood and thunderstorm wind. Our method detected the comma-shaped cloud half an hour earlier than the human label, as shown in (b_1) . As time goes to (b_2) , a clear comma-shaped cloud formulated in the middle of the image, which was detected by both our method and human labels. Red dots in (b_2) showed some severe weather events happened in Tennessee and Kentucky at that time. Since the cloud patch was large, it was hard to include the whole cloud patch in one bounding box. In that case, human labels chose the middle part of the wide cloud to label the comma-shaped cloud. In comparison, our detector used two parallel bounding boxes to cover the cloud patch, as shown in (b_2) and (b_3) . Since there was only one comma-shaped cloud, our method will output a false negative in that case.

In the third case (row 3), there were two comma-shaped cloud patches from late Jan 02, 2011 to the early next day, locating at the left and the right part of the image, respectively. As for the left comma-shaped cloud in south California, our method detected this region one hour (*i.e.* two continuous satellite images) later than the human eye detection. After the region is detected, our output is highly overlapped with the labeled regions, as indicated in the left part of (c_2) and (c_3) . As for the right comma-shaped cloud on North Atlantic Ocean, our method outputted the right comma-shaped cloud one hour earlier than human labels. Our method was able to recognize the comma-shaped cloud when the cloud just began to formulate in (c_2) . At the beginning stage, human eyes cannot recognize its shape, but our method could capture that vague shape and motion information to make a correct detection.

To conclude these three case studies, the output of our method has a good proportion of overlap with the human

labels. What is more, our method can detect some comma-shaped cloud in incomplete shape, and our detections are sometimes earlier than human eyes. These good properties make it possible to use our method as a supplement of human detections in practical weather forecasting. On the other hand, our detection scheme has a shortness as indicated in case (b). It has difficulty outputting the correct position of a wide comma-shaped cloud.

VI. CONCLUSIONS

We design a new computational framework to extract the shape-aware cloud movements relates to storms. Our algorithm automatically selects the areas of interest at suitable scales and then tracks the evolving process of these selected areas. Compared with human performance, the computational algorithm provides an objective (yet agnostic) standard to the definition of comma shape. It will serve as a tool to assist meteorologists in their daily case-by-case forecasting tasks.

Shape and motion are two clues frequently used by humans to interpret comma-shaped clouds. Our framework includes both the shape and the motion features based on cloud segmentation map and correlation with motion prior map. Their effectiveness in developing automatic cloud analysis methods are validated by our experiments. Further, considering the high variability of cloud appearance in satellite images affected by seasonal, geographical and temporal factors, we take a learning-based approach to enhance the robustness, which may also benefit from additional data.

Finally, the detection algorithm provides us a top-down opportunity to explore how severe weather happens. Our future work integrates our framework with the use of other data sources and models to make more reliable storm forecast.

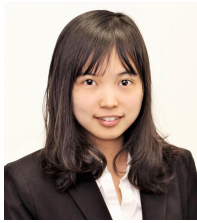
ACKNOWLEDGMENT

This material is based upon work supported in part by the National Science Foundation under Grant No. 1027854. The primary computational infrastructures used were supported by the NSF under Grant Nos. ACI-0821527 (CyberStar) and ACI-1053575 (XSEDE). We thank the National Oceanic and Atmospheric Administration (NOAA) for providing the data. Yu Zhang, Yizhi Huang, and Jianyu Mao assisted with data collection, labeling, and visualization, respectively. We would also like to thank Haibo Zhang for his feedback on this paper.

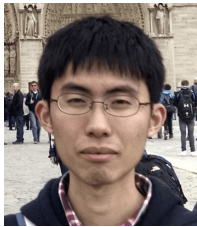
REFERENCES

- [1] "Us disaster statistics," <http://www.disaster-survival-resources.com/us-disaster-statistics.html>, [Online; accessed August-18-2017].
- [2] National Oceanic and Atmospheric Administration, "NOAA budget summary 2016," http://www.corporateservices.noaa.gov/nbo/fy16_bluebook/FY2016BudgetSummary-web.pdf, [Online; accessed August-18-2017].
- [3] —, "Thunderstorm forecasting," <http://www.nssl.noaa.gov/education/srvwx101/thunderstorms/forecasting/>, [Online; accessed August-18-2017].
- [4] T. N. Carlson, "Airflow through midlatitude cyclones and the comma cloud pattern," *Monthly Weather Review*, vol. 108, no. 10, pp. 1498–1509, 1980.
- [5] R. J. Reed, "Cyclogenesis in polar air streams," *Monthly Weather Review*, vol. 107, no. 1, pp. 38–52, 1979.
- [6] J. Li and J. Z. Wang, "Automatic linguistic indexing of pictures by a statistical modeling approach," *IEEE Transactions on Pattern Analysis and Machine Intelligence*, vol. 25, no. 9, pp. 1075–1088, 2003.
- [7] —, "Real-time computerized annotation of pictures," *IEEE Transactions on Pattern Analysis and Machine Intelligence*, vol. 30, no. 6, pp. 985–1002, 2008.
- [8] V. Lakshmanan, R. Rabin, and V. DeBrunner, "Multiscale storm identification and forecast," *Atmospheric Research*, vol. 67, pp. 367–380, 2003.
- [9] V. Lakshmanan, K. Hondl, and R. Rabin, "An efficient, general-purpose technique for identifying storm cells in geospatial images," *Journal of Atmospheric and Oceanic Technology*, vol. 26, no. 3, pp. 523–537, 2009.
- [10] J. A. Leese, C. S. Novak, and V. R. Taylor, "The determination of cloud pattern motions from geosynchronous satellite image data," *Pattern Recognition*, vol. 2, no. 4, pp. 279–292, 1970.
- [11] E. A. Smith and D. R. Phillips, "Automated cloud tracking using precisely aligned digital ats pictures," *IEEE Transactions on Computers*, vol. 100, no. 7, pp. 715–729, 1972.
- [12] A. N. Evans, "Cloud motion analysis using multichannel correlation-relaxation labeling," *IEEE Geoscience and Remote Sensing Letters*, vol. 3, no. 3, pp. 392–396, 2006.
- [13] J. Johnson, P. L. MacKeen, A. Witt, E. D. W. Mitchell, G. J. Stumpf, M. D. Eilts, and K. W. Thomas, "The storm cell identification and tracking algorithm: An enhanced WSR-88D algorithm," *Weather and Forecasting*, vol. 13, no. 2, pp. 263–276, 1998.
- [14] R. Rinehart and E. Garvey, "Three-dimensional storm motion detection by conventional weather radar," *Nature*, vol. 273, no. 5660, pp. 287–289, 1978.
- [15] R. M. Endlich and D. E. Wolf, "Automatic cloud tracking applied to goes and meteosat observations," *Journal of Applied Meteorology*, vol. 20, no. 3, pp. 309–319, 1981.
- [16] L. M. Carvalho and C. Jones, "A satellite method to identify structural properties of mesoscale convective systems based on the maximum spatial correlation tracking technique (mascotte)," *Journal of Applied Meteorology*, vol. 40, no. 10, pp. 1683–1701, 2001.
- [17] R. K. Crane, "Automatic cell detection and tracking," *IEEE Transactions on Geoscience Electronics*, vol. 17, no. 4, pp. 250–262, 1979.
- [18] M. Dixon and G. Wiener, "TITAN: Thunderstorm identification, tracking, analysis, and nowcasting-A radar-based methodology," *Journal of Atmospheric and Oceanic Technology*, vol. 10, no. 6, pp. 785–797, 1993.
- [19] L. Han, S. Fu, L. Zhao, Y. Zheng, H. Wang, and Y. Lin, "3D convective storm identification, tracking, and forecasting an enhanced TITAN algorithm," *Journal of Atmospheric and Oceanic Technology*, vol. 26, no. 4, pp. 719–732, 2009.
- [20] V. Lakshmanan and T. Smith, "Data mining storm attributes from spatial grids," *Journal of Atmospheric and Oceanic Technology*, vol. 26, no. 11, pp. 2353–2365, 2009.
- [21] L. López and J. Sánchez, "Discriminant methods for radar detection of hail," *Atmospheric Research*, vol. 93, no. 1, pp. 358–368, 2009.
- [22] M. M. Kamani, F. Farhat, S. Wistar, and J. Z. Wang, "Shape matching using skeleton context for automated bow echo detection," in *IEEE International Conference on Big Data*, 2016, pp. 901–908.
- [23] K. J. Westrick, C. F. Mass, and B. A. Colle, "The limitations of the WSR-88D radar network for quantitative precipitation measurement over the coastal western united states," *Bulletin of the American Meteorological Society*, vol. 80, no. 11, pp. 2289–2298, 1999.
- [24] M. Weinreb, J. Johnson, and D. Han, "Conversion of GVAR infrared data to scene radiance or temperature," <http://www.ospo.noaa.gov/Operations/GOES/calibration/gvar-conversion.html>, 2011, [Online; accessed May-18-2017].
- [25] S.-S. Ho and A. Talukder, "Automated cyclone discovery and tracking using knowledge sharing in multiple heterogeneous satellite data," in *Proceedings of the 14th ACM SIGKDD International Conference on Knowledge Discovery and Data Mining*. ACM, 2008, pp. 928–936.
- [26] A. N. Srivastava and J. Stroeve, "Onboard detection of snow, ice, clouds and other geophysical processes using kernel methods," in *Proceedings of the ICML*, vol. 3, 2003.
- [27] R. S. Lee and J. N. Liu, "Tropical cyclone identification and tracking system using integrated neural oscillatory elastic graph matching and hybrid rbf network track mining techniques," *IEEE Transactions on Neural Networks*, vol. 11, no. 3, pp. 680–689, 2000.
- [28] S.-S. Ho and A. Talukder, "Automated cyclone identification from remote quikscat satellite data," in *IEEE Aerospace Conference*, 2008, pp. 1–9.
- [29] L. Zhou, C. Kambhamettu, D. B. Goldgof, K. Palaniappan, and A. Hasler, "Tracking nonrigid motion and structure from 2d satellite cloud images without correspondences," *IEEE Transactions on Pattern Analysis and Machine Intelligence*, vol. 23, no. 11, pp. 1330–1336, 2001.
- [30] Y. Zhang, S. Wistar, J. Li, M. A. Steinberg, and J. Z. Wang, "Severe thunderstorm detection by visual learning using satellite images," *IEEE Transactions on Geoscience and Remote Sensing*, vol. 55, no. 2, pp. 1039–1052, 2017.
- [31] A. Arking and J. D. Childs, "Retrieval of cloud cover parameters from multispectral satellite images," *Journal of Climate and Applied Meteorology*, vol. 24, no. 4, pp. 322–333, 1985.
- [32] National Oceanic and Atmospheric Administration, "Earth location users guide (ELUG)," <https://goes.gsfc.nasa.gov/text/ELUG0398.pdf>, 1998, [Online; accessed May-18-2017].
- [33] —, "NOAA Storm Events Database," <https://www.ncdc.noaa.gov/stormevents/>, [Data retrieved from NOAA website; accessed May-18-2017].
- [34] National Oceanic and Atmospheric Administration National Environmental Satellite Data Information Service, National Climatic Data Center, "Storm data select publication 2011-01 to 2012-12," <https://www.ncdc.noaa.gov/IPS/sd/sd.html>, [Online; accessed May-18-2017].
- [35] N. Otsu, "A threshold selection method from gray-level histograms," *IEEE Transactions on Systems, Man, and Cybernetics*, vol. 9, no. 1, pp. 62–66, 1979.
- [36] C. Papageorgiou and T. Poggio, "A trainable system for object detection," *International Journal of Computer Vision*, vol. 38, no. 1, pp. 15–33, 2000.
- [37] M. Everingham, L. Van Gool, C. K. I. Williams, J. Winn, and A. Zisserman, "The PASCAL Visual Object Classes Challenge 2012 (VOC2012) Results," <http://www.pascal-network.org/challenges/VOC/voc2012/worksop/index.html>, [Online; accessed August-18-2017].
- [38] N. Dalal and B. Triggs, "Histograms of oriented gradients for human detection," in *IEEE Computer Society Conference on Computer Vision and Pattern Recognition*, vol. 1, 2005, pp. 886–893.
- [39] D. H. Wolpert, "Stacked generalization," *Neural Networks*, vol. 5, no. 2, pp. 241–259, 1992.
- [40] Y. Freund and R. E. Schapire, "A decision-theoretic generalization of on-line learning and an application to boosting," in *European Conference on Computational Learning Theory*. Springer, 1995, pp. 23–37.
- [41] E. Rosten and T. Drummond, "Machine learning for high-speed corner detection," in *European Conference on Computer Vision*. Springer, 2006, pp. 430–443.

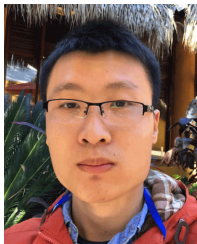
- [42] R. E. Stewart and S. R. Macpherson, "Winter storm structure and melting-induced circulations," *Atmosphere-Ocean*, vol. 27, no. 1, pp. 5–23, 1989.
- [43] C. Morel and S. Senesi, "A climatology of mesoscale convective systems over europe using satellite infrared imagery. i: Methodology," *Quarterly Journal of the Royal Meteorological Society*, vol. 128, no. 584, pp. 1953–1971, 2002.
- [44] T. Fiolleau and R. Roca, "An algorithm for the detection and tracking of tropical mesoscale convective systems using infrared images from geostationary satellite," *IEEE Transactions on Geoscience and Remote Sensing*, vol. 51, no. 7, pp. 4302–4315, 2013.
- [45] P. J. Rousseeuw, "Silhouettes: a graphical aid to the interpretation and validation of cluster analysis," *Journal of Computational and Applied Mathematics*, vol. 20, pp. 53–65, 1987.



Xinye Zheng received the bachelors degree in Statistics from the University of Science and Technology of China in 2015. She is currently a PhD candidate and Research Assistant at the College of Information Sciences and Technology, The Pennsylvania State University. Her research interests include data mining, statistical modeling, big visual data, and their applications in meteorology.



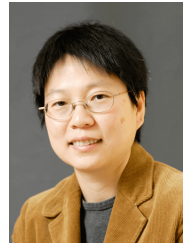
(2013-2018). His research interests include statistical modeling and learning, numerical optimization and method, and affective image modeling.



Yikun Chen received the bachelors degree in Applied Physics from the University of Science and Technology of China in 2014. He is currently a PhD candidate and Research Assistant at the College of Information Sciences and Technology, The Pennsylvania State University. He has been a summer intern at Google in 2017.



Stephen Wistar is a Certified Consulting Meteorologist (CCM) and Senior Forensic Meteorologist. He has worked on numerous cases involving Hurricane Katrina, building collapses, flooding and slip and falls. His work involves explaining meteorology to the non-scientist. At AccuWeather, Steve constructs impartial scientific weather evidence for use in courts of law to support the prosecution, which has aided Steve in testifying over 125 times in courtrooms or depositions. Furthermore, he coordinates numerous past weather research projects using forensic meteorology, like the 250 reports Steve wrote on the impacts of Hurricane Katrina at specific locations on Gulf Coast.



Jia Li is a Professor of Statistics at The Pennsylvania State University. She received the MS degree in Electrical Engineering, the MS degree in Statistics, and the PhD degree in Electrical Engineering, all from Stanford University. She worked as a Program Director in the Division of Mathematical Sciences at the National Science Foundation from 2011 to 2013, a Visiting Scientist at Google Labs in Pittsburgh from 2007 to 2008, a researcher at the Xerox Palo Alto Research Center from 1999 to 2000, and a Research Associate in the Computer Science Department at Stanford University in 1999. Her research interests include statistical modeling and learning, data mining, computational biology, image processing, and image annotation and retrieval.



problems.

Jose A. Piedra-Fernández received the Bachelors degree in computer science and the M.S. and Ph.D. degrees from the University of Almerá, Almerá, Spain, in 2001, 2003, and 2005, respectively. He is currently an Assistant Professor at the University of Almerá. He visited the College of Information Sciences and Technology, The Pennsylvania State University, University Park, PA, USA, in 2008-2009. His main research interests include image processing, pattern recognition, and image retrieval. He has designed a hybrid system applied to remote sensing



Michael A. Steinberg received the BS in atmospheric sciences from Cornell University and the MS degree in meteorology from The Pennsylvania State University. He is an Expert Senior Meteorologist, Senior Vice President and Emeritus member of the Board of Directors of AccuWeather, Inc., where he has been employed since 1978. In this role, he interacts in a wide variety of scientific, tactical and strategic areas. He is a Fellow of the American Meteorological Society (AMS) and was a recipient of their 2016 Award for Outstanding Contribution to the Advance of Applied Meteorology for numerous, visionary innovations and accomplishments in meeting public and industrial needs for weather information. He has been a recipient of research grants from the NASA Small Business Innovation Research program and the Ben Franklin/Advanced Technology Center of Pennsylvania, and is the inventor or co-inventor on numerous patents related to weather indices and location-based services.



James Z. Wang is a Professor of Information Sciences and Technology at The Pennsylvania State University. He received the bachelors degree in mathematics and computer science *summa cum laude* from the University of Minnesota, and the MS degree in mathematics, the MS degree in computer science and the PhD degree in medical information sciences, all from Stanford University. His research interests include image analysis, image modeling, image retrieval, and their applications. He was a visiting professor at the Robotics Institute at Carnegie Mellon University (2007-2008), a lead special section guest editor of the IEEE Transactions on Pattern Analysis and Machine Intelligence (2008), and a program manager at the Office of the Director of the National Science Foundation (2011-2012). He was a recipient of a National Science Foundation Career award (2004).